Eurasia Specialized Veterinary Publication

International Journal of Veterinary Research and Allied Science

ISSN:3062-357X

2024, Volume 4, Issue 2, Page No: 112-123

Available online at: www.esvpub.com/

Near-Infrared Spectroscopy Enables Accurate Classification of Pathological Pig Lung Lesions: A Proof-of-Concept Study

Freja Pedersen[1*], Emil Kristensen[1], Clara Andersen[1]

[1]Department of Veterinary and Animal Sciences, Faculty of Health and Medical Sciences, University of Copenhagen, Frederiksberg, Denmark.

***E-mail** ✉ freja.pedersen@hotmail.com

ABSTRACT

Respiratory illnesses represent a major challenge in modern pig production, leading to notable economic losses and heightened antimicrobial usage. Reliable differentiation of lung lesions is essential for accurate diagnosis and effective disease control. The incorporation of fast, non-invasive technologies could significantly improve the management of such issues. This research explored the feasibility of employing near-infrared (NIR) spectroscopy to classify porcine lung tissue. Spectral data (908–1676 nm) from 101 lungs collected from weaned pigs were obtained using a portable device and analyzed through multivariate statistical techniques. Two distinct discriminant models were designed to distinguish between normal (N), congested (C), and pathological (P) lungs, as well as among catarrhal bronchopneumonia (CBP), fibrinous pleuropneumonia (FPP), and interstitial pneumonia (IP) forms. The model optimized for identifying specific pathological types yielded the highest classification performance. The main limitations emerged with C lungs, which showed a 30% misclassification rate with N and P samples, and with FPP lesions, which were incorrectly recognized as CBP in 30% of cases. Conversely, CBP and IP samples were consistently detected with accuracy, sensitivity, and precision exceeding 90%. In summary, these findings provide proof of concept for using NIR spectroscopy to distinguish and classify porcine lungs with various lesions, supporting future rapid and efficient diagnostic applications.

Keywords: Near-infrared spectroscopy, Porcine pneumonia, Respiratory complex, Necropsy, Veterinary pathology

Received: 16 August 2024
Revised: 12 November 2024
Accepted: 14 November 2024

How to Cite This Article: Pedersen F, Kristensen E, Andersen C. Near-Infrared Spectroscopy Enables Accurate Classification of Pathological Pig Lung Lesions: A Proof-of-Concept Study. Int J Vet Res Allied Sci. 2024;4(2):112-23. https://doi.org/10.51847/n1QAeTZUOy

Introduction

Porcine respiratory disease complex (PRDC) is a key factor contributing to economic losses and increased antimicrobial dependency in pig production systems, severely affecting both health and welfare. The interplay of environmental, genetic, and management-related factors weakens pulmonary and systemic defenses, promoting the development of polymicrobial pneumonia [1]. Primary agents such as porcine reproductive and respiratory syndrome virus (PRRSV), swine influenza virus (SIV), porcine circovirus type 2 (PCV2), pseudorabies virus (PRV), and bacteria, including Mycoplasma hyopneumoniae and Actinobacillus pleuropneumoniae, facilitate secondary infections by Pasteurella multocida, Trueperella pyogenes, Mycoplasma spp., Glaesserella parasuis, and Streptococcus suis [2, 3]. Consequently, the nature of lung lesions depends on both the pathogens involved and the host's immune competence, as well as treatment effectiveness.

Given the multifactorial etiology of PRDC, an integrated, multidisciplinary diagnostic approach is required. Clinical, epidemiological, and ante-mortem data should be combined with necropsy results [4, 5]. Gross pathology remains valuable in determining appropriate laboratory investigations, including bacterial, viral, and molecular analyses [6]. Categorizing pulmonary lesions according to their morphological features helps narrow differential

diagnoses, although overlapping or mixed patterns are common, and single pathogens can induce diverse lesions [4]. Histopathology, in turn, provides detailed insights into the underlying disease processes and, in some instances, confirms causative relationships between specific pathogens and lesions [4].

Among the principal morphopathological patterns, catarrhal bronchopneumonia (CBP), fibrinous pleuropneumonia (FPP), and interstitial pneumonia (IP) are most frequently observed at necropsy. CBP commonly occurs in infections caused by M. hyopneumoniae, though similar changes may result from other organisms [7]. FPP typically correlates with A. pleuropneumoniae infection but may also arise from Actinobacillus suis or virulent P. multocida strains linked to pleuritic inflammation [4, 8]. IP, on the other hand, is mainly associated with viral agents such as PRRSV and PCV2 [6].

The rapid and precise differentiation of these lesion types is critical for selecting appropriate diagnostic tests. While gross and microscopic evaluations are essential for morphological diagnosis, incorporating objective, fast, and non-destructive analytical tools can considerably enhance diagnostic confirmation within short timeframes. Implementing these technologies in abattoirs and veterinary diagnostic facilities could accelerate inspection and analysis, decrease manual workload, and optimize disease monitoring. Such systems also have the potential to improve the assessment of animal health and welfare in slaughterhouses, which serve as vital checkpoints for evaluating respiratory disease prevalence in pig herds [9–11].

Over time, several lung lesion scoring methods have been developed for slaughter pigs, helping veterinarians and producers evaluate preventive and management strategies [12–14]. These scoring systems usually assess lesion extent and severity through visual and tactile inspection, particularly focusing on bronchopneumonia and chronic pleuritis [15]. The use of novel non-invasive methods in slaughter settings, in accordance with Regulation (EU) 625/2017 [16], could reinforce veterinary inspection efficiency and enhance food safety, public health, and animal welfare surveillance at abattoirs [17, 18]. Furthermore, technologies capable of continuously and objectively classifying pulmonary inflammatory patterns would offer an accurate overview of respiratory health status within farms and provide more detailed feedback to herd veterinarians, thereby improving PRDC management [19].

Near-infrared (NIR) spectroscopy has become a widely recognized analytical approach, demonstrating reliability across various sectors such as agriculture, food science, and pharmaceuticals. The technique operates on the principle of detecting the interaction between NIR electromagnetic radiation and molecular structures within a sample. This interaction produces a distinctive spectral profile that contains detailed information about the composition and physical state of the examined tissue [20]. In theory, these spectral profiles can be used to rapidly identify unique signatures associated with different lung lesions, enabling fast and precise recognition of pathological alterations while reducing operational time and costs.

NIR spectroscopy has gained substantial attention in human medicine [21], especially in detecting pathological changes in renal tissues and fibrotic or steatotic liver disorders [22–24]. Its adaptability has also been validated in veterinary diagnostics and meat quality assessment. Applications combining NIR and ultraviolet-visible (UV) spectroscopy, often within hyperspectral imaging systems, have effectively differentiated normal and septicemic poultry carcasses, distinguished various myopathies in poultry [25–28], identified “milk spot” livers [29], and separated healthy from diseased ovine lung samples [30].

Based on these advancements, the main objective of the current study was to evaluate, for the first time, the feasibility of using portable NIR spectroscopy as a novel method for assessing pulmonary lesions in pigs. This work represents a pioneering step toward demonstrating the potential of this technology within veterinary pathology.

The results presented here mark an initial outcome of a continuing research initiative focused on the creation and implementation of objective analytical systems combining NIR spectroscopy with computer vision tools. These systems are designed to enhance postmortem evaluation of pig carcasses and organs, as well as assist in diagnostic applications.

Materials and Methods

Lung samples

A total of 101 lungs were obtained from weaned pigs weighing less than 50 kg, submitted for postmortem investigation to the Diagnostic Section of the Istituto Zooprofilattico Sperimentale della Lombardia e dell’Emilia Romagna (IZSLER), Brescia, Italy. Only lungs in good preservation condition were used to prevent the inclusion of samples showing postmortem degradation.

Each lung underwent a detailed visual and palpatory assessment by experienced veterinarians to establish a gross morphological diagnosis. Three acute pneumonia patterns—catarrhal bronchopneumonia (CBP), fibrinous pleuropneumonia (FPP), and interstitial pneumonia (IP)—were identified according to the classification system proposed by Ruggeri *et al*. [6]. Briefly, CBP typically shows a cranioventral distribution, mainly affecting apical, middle, and cranial diaphragmatic lobes. In acute forms, the tissue appears firm, consolidated, and dark red-purple, with white catarrhal exudate visible within airways.

In FPP, lesions are mainly restricted to the dorso-caudal diaphragmatic lobes. The affected parenchyma appears dark red to nearly black, moderately firm, and heterogeneously altered, with hemorrhage, widened interlobular septa, and friable necrotic foci bordered by fibrinous leukocyte layers. Fibrin coatings are often present on pleural surfaces. In contrast, IP is characterized by a diffuse distribution of lesions, with lungs failing to collapse, showing rubbery consistency and color changes ranging from pale to reddish-purple. Acute IP often presents with marked hyperemia and interlobular edema.

When available, normal (N) and congested (C) tissue areas—either from the same lung or from separate, unaffected lungs—were also included. Congested areas were defined as regions with unchanged consistency but a deeper red coloration than normal tissue. Representative macroscopic images of all examined categories are provided in **Figure 1**.

a) b) c) d) e)

Figure 1. Lung tissue types selected during necropsy. (a) normal tissue; (b) congested tissue; (c) catarrhal bronchopneumonia; (d) fibrinous pleuropneumonia; (e) interstitial pneumonia.

Near-infrared spectroscopic analysis

NIR diffuse reflectance spectra of lung samples were recorded during necropsy at 20 °C by trained veterinarians using a portable, battery-operated spectrometer (MicroNIR OnSite-W, Viavi Solutions, Santa Rosa, CA, USA). Measurements covered the 908–1676 nm wavelength range, with an apparent resolution of 6.1 nm, an integration time of 10 ms, and 100 co-added scans. Instrument calibration and background corrections were performed prior to and periodically during analysis—specifically, after every ten tissue samples—by capturing “black” (total absorbance) and “white” (total reflectance) reference spectra using Spectralon® Diffuse Reflectance Standards (Labsphere, Inc., North Sutton, NH, USA).

All visible N, C, and pathological (P) tissue regions were analyzed by positioning the device perpendicular (90°) to the lung surface, covering an area of approximately 1.5–2 cm², as depicted in **Figure 2**. For each site, eight replicate spectra were acquired to account for the intrinsic compositional variability of lung tissue. Between each acquisition, the device was slightly rotated to ensure sampling of different micro-areas.

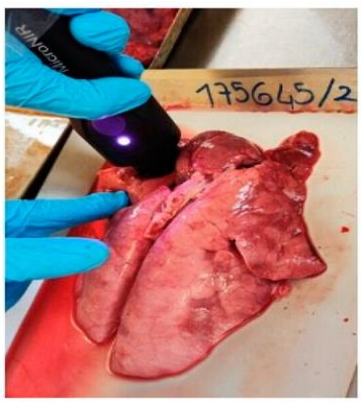

Figure 2. Recording of NIR spectra from porcine lung tissue using a portable handheld spectrometer.

NIR data processing

Prior to statistical evaluation and model construction, all NIR spectral data underwent a detailed inspection and visual screening to identify and remove possible analytical anomalies or outlier samples. After filtering, the final dataset used for multivariate processing consisted of N = 1298 spectra, categorized into specific lung tissue groups as summarized in **Table 1**, and included 125 variables, each representing absorbance measurements across the examined NIR wavelengths.

Table 1. Allocation of NIR spectra among lung tissue categories.

Lung Tissue Class	No. of Collected NIR Spectra
N	419
C	291
CBP	451
FPP	113
IP	24

The selected spectra were mean-centered and subjected to preprocessing to enhance precision and reliability in later analyses. Although the raw spectra contained valuable compositional data, they also displayed undesirable variations such as baseline drift and shifts, which could obscure subtle spectral differences essential for tissue classification. To address this, two standard preprocessing algorithms frequently applied in NIR data analysis were sequentially implemented:

- Standard Normal Variate (SNV): applied to minimize light scattering effects and compensate for baseline fluctuations.
- Fourth-Order Derivative (4Der): employed to sharpen overlapping bands and accentuate meaningful spectral features.

Multivariate statistics

Multivariate statistical analysis using Orthogonal Partial Least Squares Discriminant Analysis (OPLS-DA) was applied to the SNV + 4Der preprocessed data to construct predictive classification models capable of distinguishing between different lung tissue types. This technique established associations between the NIR spectral signatures and the reference diagnostic categories assigned by veterinary experts.

Two independent OPLS-DA models were developed:

- Model 1 (3-class): designed to differentiate among normal (N), congested (C), and pathological (P) tissues.
- Model 2 (3-class): restricted to pathological spectra, aimed at distinguishing catarrhal bronchopneumonia (CBP), fibrinous pleuropneumonia (FPP), and interstitial pneumonia (IP).

For both models, the dataset was divided randomly into calibration (75%) and validation (25%) subsets. Accordingly, Model 1 contained N = 974 calibration spectra and N = 324 validation spectra, while Model 2 included N = 441 calibration and N = 147 validation spectra. Model training was carried out with 7-fold cross-validation, while the validation sets provided independent testing data for external performance evaluation.

Confusion matrices were generated for both models to compare predicted versus actual class labels, allowing the identification of true and false positives and negatives. These outcomes were used to compute specificity, sensitivity, accuracy, and precision percentages, offering a comprehensive measure of classification performance [31].

To determine the most relevant NIR wavelengths contributing to class discrimination, the Variable Importance in Projection (VIP) index was applied, with VIP ≥ 1 indicating significant influence [32]. All multivariate procedures were executed using SIMCA® v.17.0.2.34594 (Sartorius Stedim Data Analytics AB, Umeå, Sweden).

Results and Discussion

NIR spectral profiles of lung tissues

To better visualize spectral trends, mean NIR spectra were computed for each tissue group (N, C, P, CBP, FPP, IP). The unprocessed and preprocessed (SNV + 4Der) spectra, covering the 908–1676 nm range, are illustrated in **Figures 3a and 3b**, respectively.

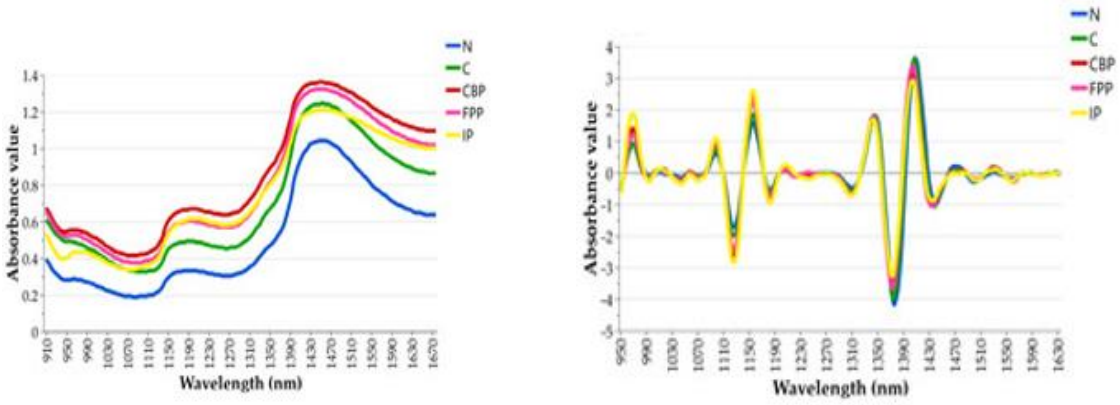

a) b)

Figure 3. Comparative plots of average NIR spectra for all lung tissue classes: (a) unprocessed spectra, (b) spectra after SNV + 4Der correction.

The raw spectra exhibited baseline variations, displacement artifacts, and broad unresolved features, rendering them unsuitable for direct interpretation **(Figure 3a)**. Conversely, preprocessing significantly enhanced resolution and pattern clarity **(Figure 3b)**. Visual examination of the corrected spectra revealed specific wavelength intervals displaying distinct absorbance variations between tissue types. Notably, IP tissues showed higher absorption in the 950–990 nm, 1070–1110 nm, and 1140–1190 nm ranges. Conversely, N and C tissues displayed stronger absorbance in the 1320–1360 nm and 1400–1430 nm regions. Minor peaks around 1460–1490 nm and 1520–1550 nm were also observed, although they appeared with comparable intensity across all groups.

Discriminant analysis

The first classification model (Model 1) was designed to separate N, C, and P lung categories through the use of OPLS-DA on the calibration dataset. This model incorporated two predictive and seven orthogonal components. As outlined in **Table 2**, both the cumulative fitting capability (R2Xcum) and predictive statistics (R2Ycum and Q2cum) exceeded 0.5, confirming that the model adequately captured the variance necessary to distinguish the three tissue groups.

Table 2. Overview of calibration parameters for the constructed discriminant models.

Model	Components (Predictive + Orthogonal)	R^2Xcum	R^2Ycum	Q^2cum
Model 1 (N vs. C vs. P)	2 + 7	0.936	0.547	0.532
Model 2 (CBP vs. FPP vs. IP)	2 + 7	0.904	0.647	0.615

In the score scatter plot, representing individual spectra within a two-dimensional plane defined by the first two predictive axes, the majority of tissue samples formed compact and well-distributed clusters **(Figure 4a)**. Despite the general separation among groups, some regions of overlap remained visible, particularly between adjacent tissue classes.

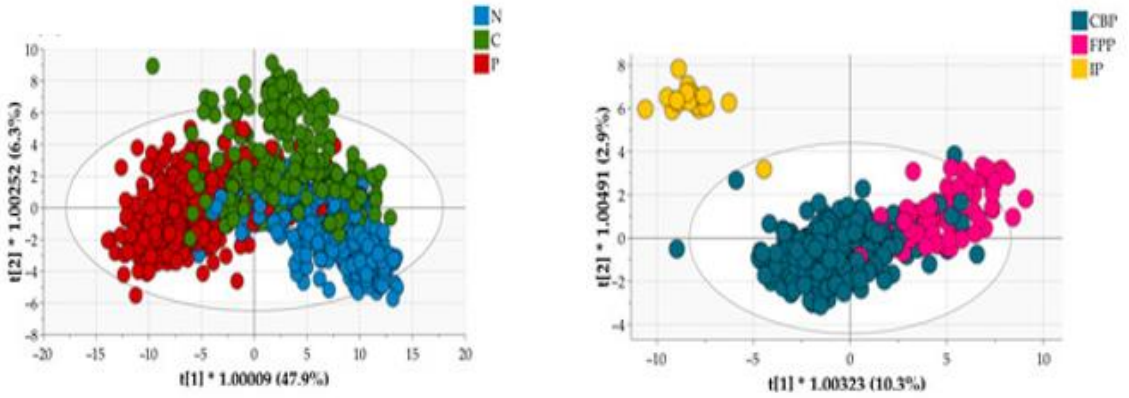

a) b)

Figure 4. OPLS-DA score scatter plots of Model 1 distinguishing N, C, and P tissues (a), and Model 2 differentiating CBP, FPP, and IP types (b), were produced through internal cross-validation of the calibration datasets.

The second discriminant model (Model 2), built to distinguish among CBP, FPP, and IP lesions, was established using the same number of predictive (2) and orthogonal (7) components. The obtained parameters were R2Xcum = 0.904, R2Ycum = 0.647, and Q2cum = 0.615 **(Table 2)**. While this model demonstrated slightly weaker fitting performance compared to Model 1, its predictive accuracy was comparatively stronger.

The score plot of Model 2 **(Figure 4b)** displayed three distinct groupings corresponding to the pneumonia variants. The IP category appeared clearly separated from the other two along both t[1] and t[2] dimensions, despite representing a smaller sample set. Only a single IP spectrum overlapped partially with the CBP group. However, certain intersections between CBP and FPP samples were still evident **(Figure 4b)**.

The Variable Importance in Projection (VIP) scores identified wavelengths most influential for class assignment, as detailed in **Table 3**. For Model 1, the most relevant signals corresponded to amide/protein (1515 nm, VIP = 1.28), water (976 nm, VIP = 1.27), and alcohol (964 nm, VIP = 1.23) bands. Additionally, bands linked to amines and fatty acids—notably at 1472, 1521, 1391, 1428, 1422, and 1327 nm—showed significant discriminative weight.

Within Model 2, the wavelengths contributing most strongly to tissue separation were located at 1580 nm (alcohol/water, VIP = 2.24), 1453 nm (water, VIP = 2.16), and 1471 nm (amide/protein, VIP = 2.06). Once again, signals associated with aliphatic hydrocarbon chains of fatty acids were evident, confirming their role in differentiating among pneumonia subtypes **(Table 3)**.

Table 3. The ten leading Variable Importance in Projection (VIP) values showing the main NIR wavelengths for distinguishing N vs. C vs. P (Model 1) and CBP vs. FPP vs. IP (Model 2) lung samples, with their respective spectral attributions *.

Model 1 (N vs. C vs. P)		
NIR Wavelength (nm)	**VIP Value**	**Assignment**
1515	1.28	Amide/protein
976	1.27	Water
970	1.24	–
964	1.23	Alkyl alcohol
1472	1.22	Aromatic amine
1521	1.22	Amide/protein
1391	1.21	Aliphatic hydrocarbon
1428	1.21	Primary amides
1422	1.20	Aromatic hydrocarbon

1397	1.20	Aliphatic hydrocarbon
Model 2 (CBP vs. FPP vs. IP)		
NIR Wavelength (nm)	**VIP Value**	**Assignment**
1580	2.24	Alcohol/water
1453	2.16	Water
1471	2.06	Amide/protein
1205	2.05	Water
1463	2.03	Amide/protein
1212	1.95	Aliphatic hydrocarbons
1023	1.95	Aromatic amines
1218	1.62	Aliphatic hydrocarbons
1042	1.48	Aliphatic hydrocarbons
1174	1.44	Alkenes

*Assignments based on [33].

Independent testing of Model 1 using the validation subset demonstrated consistent and encouraging outcomes. The model successfully recognized 84.6% of N, 69.9% of C, and 90.5% of P tissues correctly **(Table 4)**. However, in line with the overlapping trends visible in **Figure 4a**, misclassification occurred most frequently among C samples, which were sometimes labeled as either N or P.

Table 4. . Confusion matrices showing classification of lung samples across categories for the validation sets of Models 1 and 2.

Model 1 (N vs. C vs. P)				
Lung Tissue Class	**Actual Members**	**N**	**C**	**P**
N	104	88	6	10
C	73	13	51	9
P	147	4	10	133
Total	**324**	**105**	**67**	**152**
Model 2 (CBP vs. FPP vs. IP)				
Lung Tissue Class	**Actual Members**	**CBP**	**FPP**	**IP**
CBP	112	107	5	0
FPP	29	9	20	0
IP	6	0	0	6
Total	**147**	**116**	**23**	**6**

Performance statistics for Model 1 are depicted in **Figure 5a**, including accuracy, precision, specificity, and sensitivity percentages. Among the evaluated classes, P tissues displayed the highest overall results, with precision = 90.5%, accuracy = 89.8%, and sensitivity = 87.5%. High sensitivity reflected the system's strong capacity for detecting true pathological cases. The C group achieved the greatest specificity, indicating the model's competence in avoiding false-positive classification of N or P tissues as C, though the inverse misclassification remained more common.

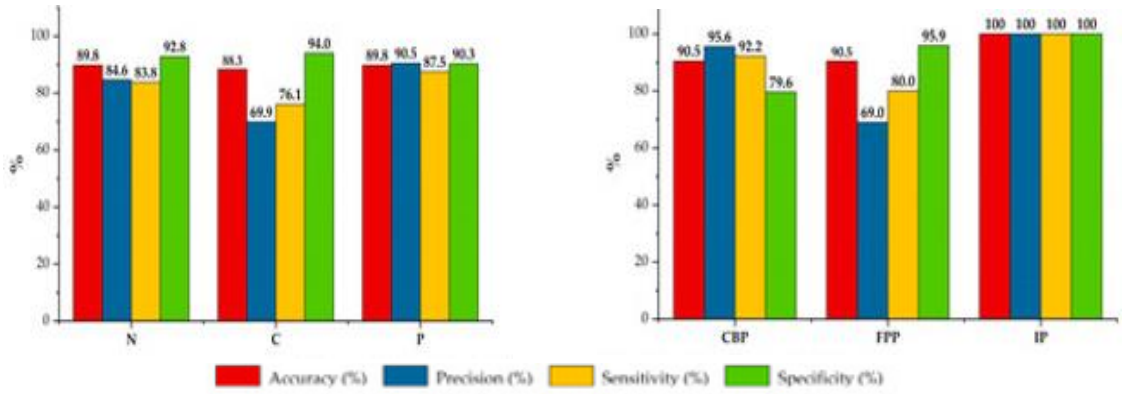

a) b)

Figure 5. Accuracy, precision, sensitivity, and specificity results from the external validation for each lung tissue type in Model 1 (N, C, P) (a) and Model 2 (CBP, FPP, IP) (b).

The independent validation of Model 2 using the testing subset yielded very favorable results. An overall precision of 90.5% was obtained in accurately detecting and assigning the unlabeled pathological lung specimens to the correct categories of CBP, FPP, or IP **(Table 4)**. On the whole, Model 2 exhibited a stronger discriminatory capability than Model 1. In particular, all lungs classified as IP were perfectly identified, with no misclassification of any CBP or FPP sample as IP, providing 100% accuracy, precision, sensitivity, and specificity for this group **(Figure 5b)**. Likewise, the model achieved high values for CBP samples, reaching 90.5% accuracy, 95.6% precision, and 92.2% sensitivity, emphasizing its excellent discriminatory performance toward this tissue type **(Table 4 and Figure 5b)**. Conversely, the FPP group exhibited a lower precision value (69.0%) **(Figure 5b)**, mainly due to the misclassification of nine FPP samples as CBP and five CBP samples being incorrectly labeled as FPP **(Table 4)**.

Although this investigation represented a preliminary phase of a broader research effort and had an exploratory focus, the obtained outcomes are encouraging, indicating the potential of NIR spectroscopy for differentiating among diverse pig lung tissue categories. The findings demonstrated that NIR spectral profiling can successfully separate N, C, and P pig lungs and also distinguish among inflammation types—CBP, FPP, and IP—thus paving the way for more efficient diagnostic and management tools for porcine respiratory disorders in veterinary applications.

In this research, the first discriminant model was built to distinguish N, C, and P samples from pig lungs, using NIR spectra acquired from these tissues (Model 1). As illustrated in **Figure 4a**, three distinctive clusters emerged for each group. The separation occurred mainly along the first predictive axis, suggesting that the model could effectively perform this differentiation. Nevertheless, partial overlaps were observed between tissue categories, pointing to the complexity of lung sample classification and the presence of shared spectral components among the studied groups.

It should be emphasized that morphological categorization in this study was performed solely through macroscopic inspection by veterinarians. Hence, the inclusion of complementary diagnostic techniques—such as histopathological examination, considered the gold standard—would likely have improved the accuracy of sample assignment, enhancing both model calibration and validation performance. Due to the heterogeneous pulmonary histoarchitecture and its variable microscopic features, the occurrence of different histological patterns within neighboring lobules is common [34]. Therefore, during NIR scanning, it is plausible that replicate spectra were captured from regions containing mixed tissue traits (e.g., overlapping N, C, and P characteristics), which could have contributed to the observed spectral overlap.

In general, the C lung spectra **(Figure 4a)** were distributed between N and P, indicating intermediate spectral properties. Pulmonary congestion, associated with increased vascular content, can arise from several factors, including passive hyperemia due to circulatory stasis or active hyperemia related to inflammatory vasodilation [35]. The enhanced blood content, rich in erythrocytes and macromolecules, explains the distinct separation of C samples from N, while their intermediate location likely mirrors the progression stages of pneumonia.

Upon external validation of Model 1, the P class displayed the highest accuracy, precision, and sensitivity values. This can be attributed to acute inflammatory alterations, including hyperemia, edema, exudate accumulation, and

leukocyte infiltration [36], which create a distinct spectral profile for P lungs, facilitating their correct classification. It should be noted that correlating NIR absorption peaks to specific chemical bonds or molecules responsible for tissue differentiation remains challenging. The VIP analysis of Model 1 revealed a complex molecular signature involved in discriminating N, C, and P categories. As indicated in **Table 3**, variations in amide, protein, water, and hydrocarbon (fatty acid) regions [33] were key contributors to tissue differentiation. These differences likely correspond to biochemical and structural alterations linked with inflammatory processes, though additional targeted studies are necessary to fully clarify these associations.

A second discriminant model was designed to classify the different inflammatory patterns in pig lungs. This model considered the three most prevalent pneumonia forms—CBP, FPP, and IP. When compared with Model 1, Model 2 showed a higher predictive performance, reinforcing the assumption that pathological alterations in tissue architecture and composition can be effectively detected through NIR spectral features. Furthermore, these findings confirm that a considerable proportion of NIR spectral variability is directly linked to the distinct pathological properties of lung tissue, supporting its use for accurate sample differentiation.

The score scatter plot for Model 2 displayed separate clusters representing each inflammation type, although partial overlap occurred between CBP and FPP samples **(Figure 4b)**. However these two pneumonia patterns are typically described as separate pathological entities; mixed lesions combining features of both conditions are frequently encountered in routine postmortem examinations. Consequently, the inclusion of histopathological verification in future work is essential to further refine the model calibration and enhance accuracy. Notably, IP samples were clearly separated from the others, and external validation yielded 100% accuracy, precision, sensitivity, and specificity for this tissue type **(Figures 4b and 5b)**. The distinct pathological mechanisms of interstitial pneumonia, when compared with the other two pneumonia forms, likely account for these results. While CBP and FPP primarily show catarrhal or fibrinous exudates and neutrophilic/macrophagic infiltration within alveolar spaces and distal bronchioles, IP mainly involves changes in the peribronchiolar, perivascular, and perilobular interstitium. In acute IP, edema and dense lymphoplasmacytic and histiocytic infiltrates expand the alveolar and interlobular septa, while chronic progression results in marked interstitial fibrosis [35].

When analyzing the NIR absorbance variations that contributed most to distinguishing the pathological groups **(Table 3)**, water absorption bands appeared as the dominant factor, followed by amide/protein signals [33]. This may indicate that exudative and inflammatory cellular processes influence the observed spectral fingerprints for these lung conditions **(Table 3)**. Nevertheless, future investigations should involve a larger sample set, especially for IP, to confirm these findings. Moreover, complementing NIR spectroscopy with other chemical or molecular analyses will be critical for a comprehensive understanding of these biological samples.

Overall results

The present study provides convincing proof of concept for employing NIR spectroscopy to classify pig lung tissue categories, opening new prospects for rapid and reliable diagnostic methodologies. The model performance metrics were highly satisfactory, closely matching those reported in earlier studies that applied NIR analysis to distinguish normal and pathological tissues. In fact, classification accuracy exceeded 90%, aligning with the performance levels documented in previous literature [26–28]. The few observed misclassifications appeared mainly linked to variability in lesion severity or a continuum between healthy and diseased tissues, echoing challenges frequently noted in prior research [26–28].

Application perspectives

In conclusion, the use of NIR spectroscopy, particularly through portable handheld devices, shows considerable promise not only in veterinary laboratory diagnostics but also in slaughterhouse inspection contexts. For instance, systematic NIR-based assessment of lung tissues during routine abattoir evaluations could yield large-scale epidemiological data and improve on-farm respiratory disease management. Nonetheless, implementing portable NIR tools in high-throughput industrial facilities entails significant technical and logistical constraints that must be carefully addressed [37]. To this end, future efforts should focus on developing advanced contactless NIR sensors capable of remote, automated tissue assessment, in line with Regulation (EU) 2019/627, which promotes a visual-only, risk-based postmortem inspection framework in pig slaughterhouses [38, 39].

Furthermore, the introduction of customized hyperspectral imaging systems functioning in the NIR range within processing lines could mark a major technological step forward. Such systems, based on principles similar to those of portable NIR devices, can operate in real time, enabling the spatial mapping of spectral features across the entire organ surface. Compared to conventional RGB cameras (limited to the 400–700 nm visible spectrum), NIR hyperspectral imaging extends data acquisition to a broader spectral range, allowing for better artifact

discrimination (e.g., those caused by carcass shape or blood residues). This capability can significantly improve the reliability of lesion detection and quality control in industrial meat inspection environments.

Conclusion

The incorporation of advanced analytical instruments is becoming a key development in animal health and veterinary diagnostics. Although NIR spectroscopy has only recently been tested for assessing pig lung pathology, the findings from this investigation clearly demonstrate its feasibility for automated and objective differentiation of normal, congested, and diseased tissues, as well as for the recognition of specific pneumonia patterns. Owing to its non-destructive, rapid, and user-friendly nature, this technique is particularly suitable for integration into slaughter line workflows, enabling semi-quantitative evaluation of lung lesions and their severity. The NIR-based classification models created here could become valuable decision-support tools for veterinary pathologists and inspectors, aiding necropsy procedures and disease surveillance. Ultimately, such advancements may foster improved respiratory disease control, promoting better animal welfare and public health protection.

Acknowledgments: None

Conflict of Interest: None

Financial Support: None

Ethics Statement: None

References

1. Opriessnig T, Giménez-Lirola LG, Halbur PG. Polymicrobial respiratory disease in pigs. Anim Health Res Rev. 2011;12(2):133–48.
2. Fablet C, Marois-Créhan C, Simon G, Grasland B, Jestin A, Kobisch M, et al. Infectious agents associated with respiratory diseases in 125 farrow-to-finish pig herds: a cross-sectional study. Vet Microbiol. 2012;157(3–4):152–63.
3. Petri FAM, Ferreira GC, Arruda LP, Malcher CS, Storino GY, Almeida HMS, et al. Associations between pleurisy and the main bacterial pathogens of the porcine respiratory diseases complex (PRDC). Animals. 2023;13(9):1493.
4. Sarli G, D'Annunzio G, Gobbo F, Benazzi C, Ostanello F. The role of pathology in the diagnosis of swine respiratory disease. Vet Sci. 2021;8(12):256.
5. Michael JY, William GVA. Respiratory system. In: Zimmerman JJ, Karriker LA, Ramirez A, Schwartz KJ, Stevenson GW, Zhang J, editors. Diseases of Swine. 11th ed. Ames: State University Press; 2019. p. 393–407.
6. Ruggeri J, Salogni C, Giovannini S, Vitale N, Boniotti MB, Corradi A, et al. Association between infectious agents and lesions in post-weaned piglets and fattening heavy pigs with porcine respiratory disease complex (PRDC). Front Vet Sci. 2020;7(1):636.
7. Pieters M, Maes D. Mycoplasmosis. In: Zimmerman JJ, Karriker LA, Ramirez A, Schwartz KJ, Stevenson GW, Zhang J, editors. Diseases of Swine. 11th ed. Ames: State University Press; 2019. p. 863–83.
8. Gottschalk M, Broes A. Actinobacillosis. In: Zimmerman JJ, Karriker LA, Ramirez A, Schwartz KJ, Stevenson GW, Zhang J, editors. Diseases of Swine. 11th ed. Ames: State University Press; 2019. p. 749–66.
9. Paz-Sánchez Y, Herráez P, Quesada-Canales Ó, Poveda CG, Díaz-Delgado J, Quintana-Montesdeoca MDP, et al. Assessment of lung disease in finishing pigs at slaughter: pulmonary lesions and implications on productivity parameters. Animals. 2021;11(12):3604.
10. García-Díez J, Saraiva S, Moura D, Grispoldi L, Cenci-Goga BT, Saraiva C. The importance of the slaughterhouse in surveilling animal and public health: a systematic review. Vet Sci. 2023;10(4):167.
11. Scollo A, Gottardo F, Contiero B, Mazzoni C, Leneveu P, Edwards SA. Benchmarking of pluck lesions at slaughter as a health monitoring tool for pigs slaughtered at 170 kg (heavy pigs). Prev Vet Med. 2017;144(1):20–8.

12. De Luca S, Zanardi E, Alborali GL, Ianieri A, Ghidini S. Abattoir-based measures to assess swine welfare: analysis of the methods adopted in European slaughterhouses. Animals. 2021;11(2):226.
13. Garcia-Morante B, Segalés J, Fraile L, Pérez de Rozas A, Maiti H, Coll T, et al. Assessment of Mycoplasma hyopneumoniae-induced pneumonia using different lung lesion scoring systems: a comparative review. J Comp Pathol. 2016;154(2–3):125–34.
14. Ghidini S, De Luca S, Rinaldi E, Zanardi E, Ianieri A, Guadagno F, et al. Comparing visual-only and visual-palpation post-mortem lung scoring systems in slaughtering pigs. Animals. 2023;13(18):2419.
15. Maes D, Sibila M, Pieters M, Haesebrouck F, Segalés J, de Oliveira LG. Review on the methodology to assess respiratory tract lesions in pigs and their production impact. Vet Res. 2023;54(1):8.
16. Regulation (EU) 2017/625; European Parliament Council of 15 March 2017 on Official Controls and Other Official Activities Performed to Ensure the Application of Food and Feed Law, Rules on Animal Health and Welfare, Plant Health and Plant Protection Products. 2017. Available online: https://eur-lex.europa.eu/legal-content/EN/TXT/PDF/?uri=CELEX:32017R0625 (accessed on 11 February 2024).
17. Blagojevic B, Nesbakken T, Alvseike O, Vågsholm I, Antic D, Johler S, et al. Drivers, opportunities, and challenges of the European risk-based meat safety assurance system. Food Control. 2021;124(1):107870.
18. Antunović B, Blagojević B, Johler S, Guldimann C, Vieira-Pinto M, Vågsholm I, et al. Challenges and opportunities in the implementation of new meat inspection systems in Europe. Trends Food Sci Technol. 2021;116(1):460–7.
19. Pessoa J, Rodrigues da Costa M, García Manzanilla E, Norton T, McAloon C, Boyle L. Managing respiratory disease in finisher pigs: combining quantitative assessments of clinical signs and the prevalence of lung lesions at slaughter. Prev Vet Med. 2021;186(1):105208.
20. Pasquini C. Near infrared spectroscopy: a mature analytical technique with new perspectives—A review. Anal Chim Acta. 2018;1026(1):8–36.
21. Sakudo A. Near-infrared spectroscopy for medical applications: current status and future perspectives. Clin Chim Acta. 2016;455(1):181–8.
22. Delrue C, De Bruyne S, Speeckaert MM. The potential use of near- and mid-infrared spectroscopy in kidney diseases. Int J Mol Sci. 2023;24(7):6740.
23. Sharma VJ, Adegoke JA, Fasulakis M, Green A, Goh SK, Peng X, et al. Point-of-care detection of fibrosis in liver transplant surgery using near-infrared spectroscopy and machine learning. Health Sci Rep. 2023;6(3):e1652.
24. Rienda I, Moro E, Pérez-Rubio Á, Trullenque-Juan R, Pérez-Guiata D, Lendl B, et al. Comparing the direct assessment of steatosis in liver explants with mid- and near-infrared vibrational spectroscopy prior to organ transplantation. Analyst. 2023;148(20):3986–91.
25. de Carvalho LM, Madruga MS, Estévez M, Badaró AT, Barbin DF. Occurrence of wooden breast and white striping in Brazilian slaughtering plants and use of near-infrared spectroscopy and multivariate analysis to identify affected chicken breasts. J Food Sci. 2020;85(9):3102–12.
26. Geronimo BC, Mastelini SM, Carvalho RH, Barbon Júnior S, Barbin DF, Shimokomaki M, et al. Computer vision system and near-infrared spectroscopy for identification and classification of chicken with wooden breast. Infrared Phys Technol. 2019;96(1):303–10.
27. Wold JP, Løvland A. NIR spectroscopic techniques for quality and process control in the meat industry. MMB. 2020;4(1):1–8.
28. Park B, Chen YR, Huffman RW. Integration of visible/NIR spectroscopy and multispectral imaging for poultry carcass inspection. J Food Eng. 1996;30(2):197–207.
29. Cugmas B, Bürmen M, Jemec J, Pernuš F, Likar B. Towards automated detection of milk spot livers by diffuse reflectance spectroscopy. J Food Eng. 2014;124(1):128–32.
30. Coombs CEO, Allman BE, Morton EJ, Gimeno M, Horadagoda N, Tarr G, et al. A preliminary investigation into the automatic detection of diseased sheep organs using hyperspectral imaging sensors. Smart Agric Technol. 2023;3(1):100122.
31. Fawcett T. An introduction to ROC analysis. Pattern Recognit Lett. 2006;27(8):861–74.
32. Andersen CM, Bro R. Variable selection in regression—a tutorial. J Chemom. 2010;24(11–12):728–37.
33. Workman J, Weyer L. Practical guide to interpretive near-infrared spectroscopy. 1st ed. Boca Raton: CRC Press; 2007. p. 1–333.

34. Scanziani E, Mandelli G, Radaelli E. Apparato respiratorio. In: Guarda F, Mandelli G, Biolatti B, Scanziani E, editors. Trattato di anatomia patologica veterinaria. 4th ed. Torino: UTET; 2013. p. 297–344.
35. Caswell JL, Williams KJ. Respiratory system. In: Maxie MG, editor. Jubb, Kennedy, and Palmer's pathology of domestic animals. 6th ed. Amsterdam: Elsevier; 2016. p. 465–591.
36. Ackermann MR. Inflammation and healing. In: Zachary JF, editor. Pathologic basis of veterinary disease. 6th ed. St. Louis: Elsevier; 2017. p. 73–131.
37. Kombolo-Ngah M, Goi A, Santinello M, Rampado N, Atanassova S, Liu J, et al. Across countries implementation of handheld near-infrared spectrometer for the online prediction of beef marbling in slaughterhouse. Meat Sci. 2023;200(1):109169.
38. Regulation (EU) 2019/627; Laying Down Uniform Practical Arrangements for the Performance of Official Controls on Products of Animal Origin Intended for Human Consumption in Accordance with Regulation (EU) 2017/625 of the European Parliament and of the Council and Amending Commission Regulation (EC) No 2074/2005 as Regards Official Controls. 2019. Available online: https://eur-lex.europa.eu/legal-content/EN/TXT/HTML/?uri=CELEX:32019R0627 (accessed on 11 February 2024).
39. Ghidini S, Zanardi E, Di Ciccio PA, Borrello S, Belluzi G, Guizzardi S, et al. Development and test of a visual-only meat inspection system for heavy pigs in northern Italy. BMC Vet Res. 2018;14(1):6.